Naval Research Laboratory

Washington, DC 20375-5000

NRL Memorandum Report 6734

A Computational Study of HY and HSLA Steel Performance in a Bulkhead Test Panel Geometry

VIRGINIA DEGIORGI AND PETER MATIC

Mechanics of Materials Branch
Materials Science and Technology Division

February 6, 1991

REPORT DOCUMENTATION PAGE

Form Approved
OMB No 0704-0188

1. AGENCY USE ONLY (Leave blank)	2. REPORT DATE	3. REPORT TYPE AND DATES COVERED
	1991 February 6	Final

4. TITLE AND SUBTITLE

A Computational Study of HY and HSLA Steel Performance in a Bulkhead Test Panel Geometry

5. FUNDING NUMBERS

61153N 22
RR022-01-48

6. AUTHOR(S)

Virginia DeGiorgi and Peter Matic

7. PERFORMING ORGANIZATION NAME(S) AND ADDRESS(ES)

Naval Research Laboratory
Washington, DC 20375-5000

8. PERFORMING ORGANIZATION REPORT NUMBER

NRL Memorandum
Report 6734

9. SPONSORING / MONITORING AGENCY NAME(S) AND ADDRESS(ES)

Office of Naval Research
Arlington, VA 22217

10. SPONSORING / MONITORING AGENCY REPORT NUMBER

11. SUPPLEMENTARY NOTES

12a. DISTRIBUTION / AVAILABILITY STATEMENT

Approved for public release; distribution unlimited

12b. DISTRIBUTION CODE

13. ABSTRACT *(Maximum 200 words)*

As nonlinear computational methods become integrated into the structural design and analysis process, the effects of large deformation material response on large deflection structural response can, in principle, be predicted. The accuracy of structural predictions ultimately depends on an accurate assessment of the material responses which are encountered in the structure. This is particularly true if information on locally severe plastic deformation or fracture initiation and flaw tolerance is desired. Previously determined parameters for the elastic-plastic response of HY-80, HY-100, HSLA-80 and HSLA-100 steels, accurate through large strains terminating at the point of fracture, were applied in finite element simulations to predict the performance of a bulkhead test panel geometry. Significant differences in panel performance under hydrostatic loading conditions were predicted for the materials considered. The plastic deflections were found to be strongly influenced by the relative local or diffuse nature of intense plastic deformation across the panel. These results suggest that the comparative nonlinearily of these materials was as important as the strength and ductility in affecting performance.

14. SUBJECT TERMS

Plasticity, Fracture, Finite element, Stiffened panel, Constitutive nonlinearity

15. NUMBER OF PAGES

34

16. PRICE CODE

17. SECURITY CLASSIFICATION OF REPORT	18. SECURITY CLASSIFICATION OF THIS PAGE	19. SECURITY CLASSIFICATION OF ABSTRACT	20. LIMITATION OF ABSTRACT
UNCLASSIFIED	UNCLASSIFIED	UNCLASSIFIED	UL

CONTENTS

A COMPUTATIONAL STUDY OF HY AND HSLA STEEL PERFORMANCE IN A BULKHEAD TEST PANEL GEOMETRY

Introduction

Accurate prediction of structural performance during design can ensure superior operational capability, economy and life cycle management as part of an overall optimization effort. An important part of this process for the designer is to evaluate candidate materials for use in structural components. Such an evaluation generally benefits from an understanding of how one candidate material produces enhanced component performance when compared to other candidate materials. Nonlinear computational methods are increasingly capable of providing the necessary predictions when an ability to sustain large strain deformation is desired. Such predictions require an adequate constitutive formulation and accurate constitutive parameters for the materials under consideration.

The development of different high strength, high ductility and high fracture toughness materials, such as HY-80, HY-100, HY-130, HSLA-80 and HSLA-100, provide a wide range of current choices for naval applications. For the case of hydrostatically loaded components, optimal material selection may benefit if the deformations leading to component fracture and ultimate failure can be identified, understood and employed to achieve superior structural performance.

In this investigation, a T-stiffened bulkhead test panel geometry subjected to hydrostatic loading was analyzed using nonlinear finite element methods. The comparative global and local performance of HY-80, HY-100, HSLA-80 and HSLA-100 was evaluated. Of particular interest in this study were the effects of these different materials on the relative hydrostatic pressure loads, plastic deformation and energy dissipation of the panel. Despite the important role of HY-80 and HSLA-80 yield stress as compared to HY-100 and HSLA-100 yield stress in affecting panel pressure versus deflection response, the material constitutive nonlinearity.at larger plastic strains was found to be the dominant factor affecting panel deflection and energy absorbing capabilities. At the same time, the local stress, plastic strain and energy density fields of the system at critical locations provided insight into specific factors which ultimately govern the performance of the panel geometry.

Manuscript approved October 26, 1990

Approach

A series of nonlinear finite element simulations was performed to assess the performance of HY-80, HY-100, HSLA-80 and HSLA 100 in a reinforced bulkhead test panel geometry. The panel itself (Figure 1) was designed to be welded into a circular test frame. The reinforcement on the circular plate, of thickness t_1 and diameter d_1, was provided by an inscribed square pattern of T-stiffeners of dimension s_1 on a side. The stiffener web was of thickness t_2 and height h_2. The stiffener flange was of thickness t_3 and width w_3. The flange was eccentrically positioned on the web. The inscribed square region bounded by the stiffeners is effectively the test zone of the panel. The panel is loaded hydrostatically from the stiffened side.

$\frac{r_1}{t_1} = 43.53$

$\frac{h_2}{t_2} = 16.84$

$\frac{w_3}{t_3} = 6.22$

$\frac{w_3'}{w_3} = 0.22$

$\frac{w_3''}{w_3} = 0.78$

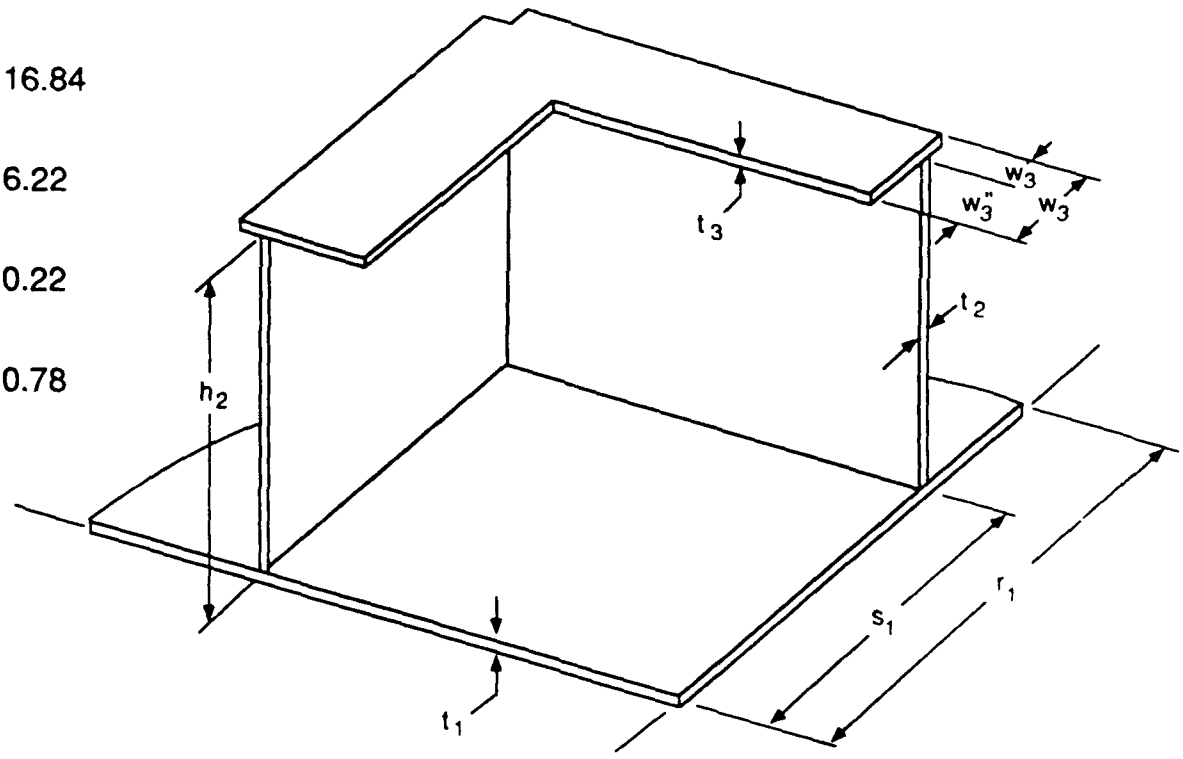

Fig. 1 — Bulkhead test panel geometry showing circular plate and square T-frame stiffener. The entire assembly was welded into a circular fixture. Hydrostatic pressure was applied from the stiffened side.

The global integrity of the panel, for the purposes of this investigation, will be defined with respect to fracture initiation. Alternative definitions of global panel integrity can, of course, be defined as needed. Examples might include a requirement to sustain a specified hydrostatic pressure or a requirement to ensure no fluid or gas leakage across the panel. Regardless of the specific performance requirement, the extent of local plastic deformation and resistance to fracture contribute to overall performance.

For the bulkhead test panel the global nonlinear deformation occurs at the panel scale. Local conditions leading to fracture occur on a scale comparable with the plate thickness. For this reason, the panel analysis for each material was performed in two steps. A global bulkhead test panel model was analyzed using shell elements. A two-dimensional plane strain model of the most severely deformed cross section detail (Figure 2) was analyzed in another model using continuum elements and boundary conditions derived from the shell element model. Plate material was included approximately seven times the plate thickness interior to the stiffener boundary and twelve times the plate thickness exterior to the stiffener boundary, i.e. to the plate periphery. Web material was included approximately four times the web thickness from the intersection. In this manner, important aspects of the panel performance at large and small spatial scales which differed by more than a factor of ten were accounted for.

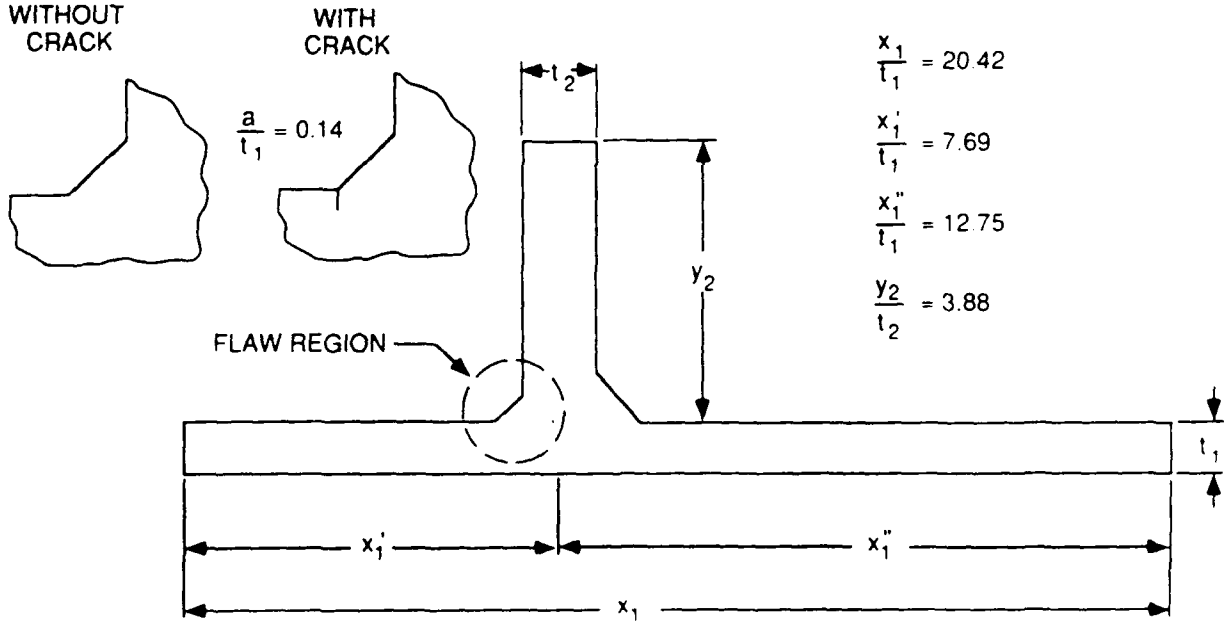

Fig. 2 — Detail of T-frame stiffener and plate intersection geometry. Displacement loading, generated from bulkhead test panel model results, was applied at material boundaries of the detail model.

The principle objectives of this investigation were to (i) assess the relative plastic deformation each material produces in the panel, (ii) understand the global mechanisms which influence the extent of plastic flow, (iii) examine the local material stress, strain and energy dissipation fields in the test panel where failure may be expected and (iv) determine the required local material toughness for evenly matched weld material for a desired hydrostatic pressure.

Material Model and Parameters for Analyses

An incremental rate independent plasticity theory in the ABAQUS finite element program [1] was used for the material constitutive model. This standard model for plasticity is summarized here for completeness. Total strains in the multiaxial strain state ε_{ij} were obtained by the integration of the linearly decomposed rate of deformation tensor D_{ij}. This integration was performed under the assumption that the elastic strains remain infinitesimal, as is the case for the HY-80, HY-100, HSLA-80 and HSLA-100 steels considered in this investigation. The total multiaxial strain state ε_{ij}, expressed in terms of elastic and plastic components, was

$$\varepsilon_{ij} = \varepsilon^{e}_{ij} + \varepsilon^{p}_{ij} \qquad (1)$$

The total logarithmic uniaxial strain ε, consistent with the integration of the rate of deformation tensor for a multiaxial strain state, was decomposed as

$$\varepsilon = \varepsilon^{e} + \varepsilon^{p} \qquad (2)$$

The yield function f takes the form

$$f(\tau_{ij}) = \tau(\varepsilon^{p}) \qquad (3)$$

where τ_{ij} and τ are the multiaxial Kirchoff (or Treffetz) and uniaxial stress states, respectively. The associated flow rule governed plastic strain increments by the relation

$$d\varepsilon^{p}_{ij} = \lambda \frac{\partial f}{\partial \tau_{ij}} \qquad (4)$$

In the case of purely elastic behavior $\lambda = 0$. For active material yielding

$$\lambda > 0 \tag{5}$$

$$\lambda = d\varepsilon^p \frac{\tau}{\tau_{ij} \dfrac{\partial f}{\partial \tau_{ij}}} \tag{6}$$

Plastic strain increments also satisfied a dissipation equivalence condition

$$\tau \, d\varepsilon^p = \tau_{ij} \, d\varepsilon^p_{ij} \tag{7}$$

and a consistency condition

$$\frac{\partial f}{\partial \tau_{ij}} d\tau_{ij} - \frac{\partial \tau}{\partial \varepsilon^p} d\varepsilon^p = 0 \tag{8}$$

The von Mises yield function

$$f(\tau_{ij}) = (\frac{3}{2} s_{ij} s_{ij})^{\frac{1}{2}} \tag{9}$$

was employed. The deviatoric stress tensor s_{ij} was defined as

$$s_{ij} = \tau_{ij} - \frac{1}{3} \tau_{kk} \delta_{ij} \tag{10}$$

where the hydrostatic component of stress is $\tau_{kk}/3$.

The Kirchoff stress and logarithmic strain measures are employed because of advantages gained in computational implementation. The Kirchoff stress tensor τ_{ij} is approximately equal to the more physically motivated Cauchy stress tensor σ_{ij} for deformations involving only small changes in volume. This condition was implicit in these analyses. The uniaxial Cauchy stress - log strain constitutive response of the materials were formally input, in multilinear form, as Cauchy stress and logarithmic strain pairs for the ABAQUS program (Figure 3). These responses, with demonstrated accuracy to the point of material fracture, were determined in previous

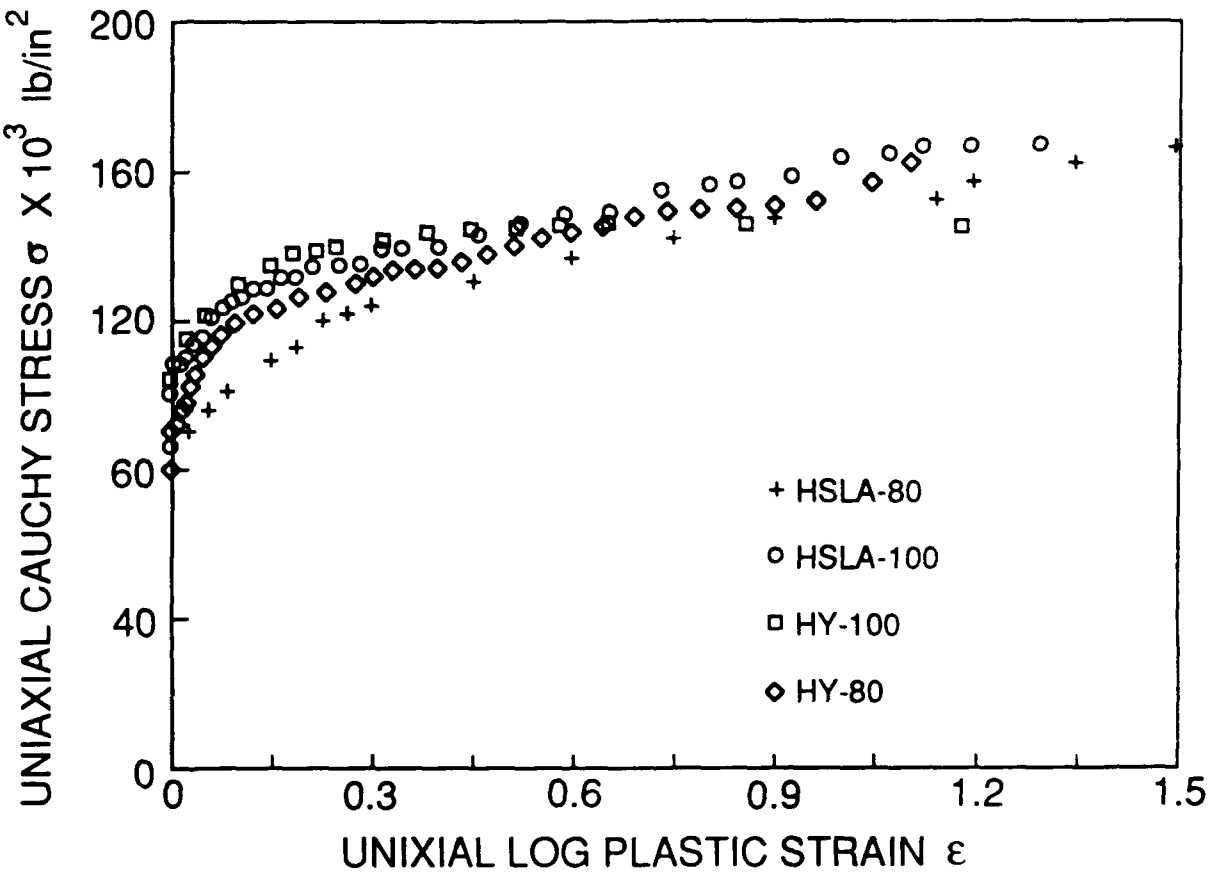

Fig. 3 — Uniaxial representation of Cauchy stress-logarithmic strain response for incremental elastic-plastic constitutive model of HY-80, HY-100, HSLA-80 and HSLA-100 materials

investigations by Wong, Kirby and Matic [2] for HY-80, Matic, Kirby and Jolles [3] for HY-100, Matic, Father, Kirby and Jolles [4] for HSLA-80 and Wong, Kirby and Matic [5] for HSLA-100.

The strain energy density per unit mass w of the material will be

$$w = \lim_{\Delta V \to 0} \left[\frac{1}{\rho} \frac{\Delta W}{\Delta V} \right] \tag{11}$$

where W is energy and V is volume. In terms of the stress components σ_{ij}, strain components ε_{ij} and the mass density ρ the strain energy density is

$$w = \int_0^{\varepsilon} \frac{\sigma_{ij}}{\rho} d\varepsilon_{ij} \tag{12}$$

The strain energy density incorporates the contributions of stress and strain quantities to the material history. The value of the energy density corresponding to local fracture of the material will be

$$w_c = \int_0^{(\varepsilon)_c} \frac{\sigma_{ij}}{\rho} d\varepsilon_{ij} \tag{13}$$

where w_c is the critical strain energy density value for a given stress-strain history. The value of w_c is generally path dependent, although a representative value may be practical for engineering application.

For ductile metals, the mass density varies only slightly, even over large deformations. For this reason, it is common to define an energy per unit volume density

$$w = \lim_{\Delta V \to 0} \left[\frac{\Delta W}{\Delta V} \right] \tag{14}$$

or

$$w=\int_0^{\varepsilon_{ij}} \sigma_{ij} d\varepsilon_{ij} \tag{15}$$

and an associated critical value

$$w_c=\int_0^{(\varepsilon_{ij})_c} \sigma_{ij} d\varepsilon_{ij} \tag{16}$$

The energy per unit mass is fundamental, but the energy per unit volume is equally appropriate for constant volume deformation processes.

For the case of a uniaxial representation of true stress versus true strain material response, the critical energy density corresponds to the area under the uniaxial stress-strain curve, i.e.

$$w_c=\int_0^{\varepsilon_c} \sigma d\varepsilon \tag{17}$$

This representation is suitable for use with traditional constitutive formulations which rely on uniaxial stress-strain curves for material data.

For a multiaxial state of stress, each of the six stress-strain pairs, three normal and three shear, must be evaluated and summed, i.e.

$$\begin{aligned} w_c=&\int_0^{(\varepsilon_{11})_c} \sigma_{11} d\varepsilon_{11} + \int_0^{(\varepsilon_{22})_c} \sigma_{22} d\varepsilon_{22} + \\ &+\int_0^{(\varepsilon_{33})_c} \sigma_{33} d\varepsilon_{33} + \int_0^{(\varepsilon_{12})_c} \sigma_{12} d\varepsilon_{12} + \\ &+\int_0^{(\varepsilon_{23})_c} \sigma_{23} d\varepsilon_{23} + \int_0^{(\varepsilon_{31})_c} \sigma_{31} d\varepsilon_{31} \end{aligned} \tag{18}$$

It should be noted that one or more individual terms, but not all six terms, in the multiaxial expression can be negative. Their total, w_c, must be positive, however.

Prediction of fracture initiation employing a local criterion requires the identification of local maximum energy densities and comparison of these maxima with a local critical energy density value. For a materially inhomogeneous component, the maximum local energy densities in each constituent material must be identified and compared with the corresponding local fracture toughness value. For a materially homogeneous component, as considered in this investigation, one critical energy density value was used to characterize local fracture resistance. Only the global maximum energy density must be identified at each increment of the loading history.

The location of the energy density maxima may vary during the loading history. Additional deformation can be sustained without fracture as long as

$$w < w_c. \tag{19}$$

Local fracture coincides with the energy density attaining the critical energy density value for the material, i.e.

$$w = w_c. \tag{20}$$

The critical energy density values used in this investigation, as obtained from the constitutive characterization references cited above, reflect conservative engineering estimates of the fracture toughness in view of the multiaxial deformation history dependence of w_c. The critical energy density values used were: 1.39×10^5 lb-in/in^3 for HY-80, 1.29×10^5 lb-in/in^3 for HY-100, 2.02×10^5 lb-in/in^3 for HSLA-80 and 2.02×10^5 lb-in/in^3 for HSLA-100.

Bulkhead Test Panel Shell Model

A finite element model of the bulkhead test panel was created using the ABAQUS finite element program [6]. Version 4-7 of the program was used for all analyses in this investigation (Figure 4). The symmetry of the reinforced panel suggested that

one-quarter of geometry was sufficient for modeling purposes. The plate, stiffener web and stiffener flange were modeled using type S8R and type STRI3 shell elements. The S8R elements are eight node, reduced integration, doubly curved quadrilateral shell elements. The STRI3 elements are three node triangular facet shell elements. Both element types feature three translational and three rotational degrees of freedom at each node. The formulation of the S8R elements is a thick shell, allowing for transverse shear stresses, with thin shell behavior in the limit. The STRI3 is a thin shell which does not account for transverse shear. The model contained 538 nodes composed into 169 elements. The S8R elements represented 145 of the elements in the model. The STRI3 elements were used in 24 element locations, primarily as geometric transitions between quadrilaterals. The total number of degrees of freedom in the model was 3228.

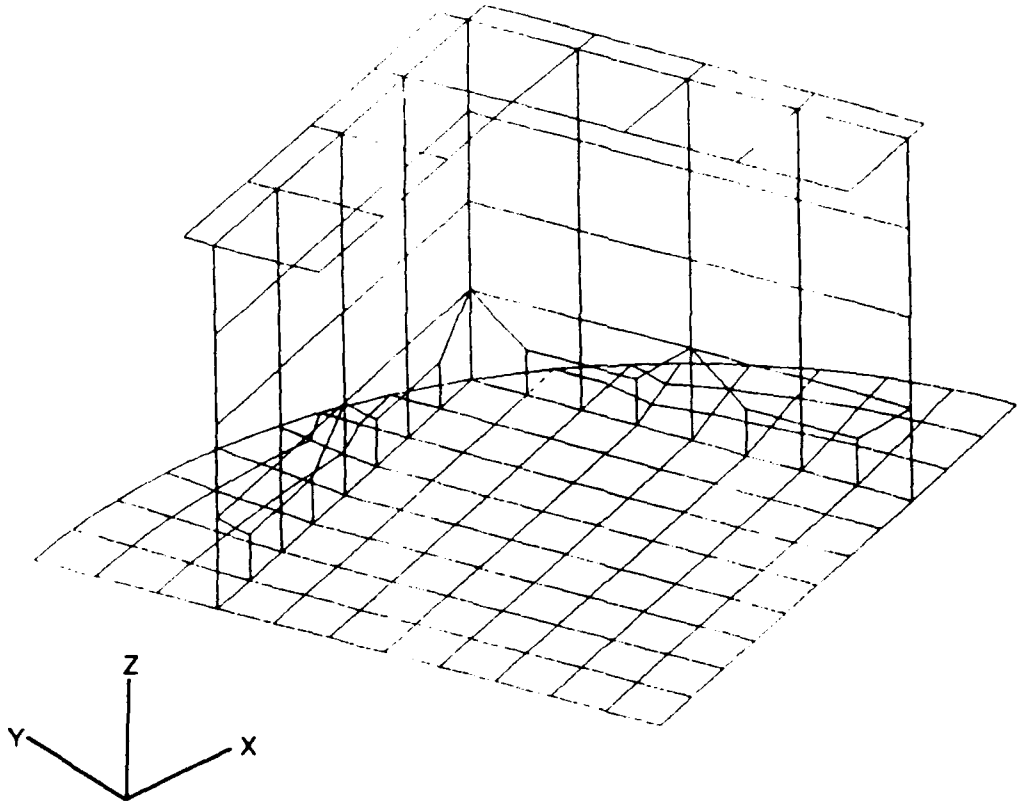

Fig. 4 — Finite element model of bulkhead test panel geometry utilizing symmetry about x and y axes

The test fixture at the periphery of the plate was considered to be much stiffer than the bulkhead test panel and was not modeled. Zero displacement and zero rotation boundary conditions were specified around the circular periphery of the plate in the model. This effectively accounted for the welding of the test panel into the test fixture in the simulation.

Pressure loads were applied to the stiffened side of the panel surface to simulate hydrostatic loading. Pressure loads were not applied to the web or flange surfaces since they produced no membrane or bending stresses in either plate, web or flange components. The compressive stresses produced by such self-equilibrating pressures in the web and flange were small in comparison to the stresses produced by pressure loads on the plate.

Bulkhead Test Panel Model Results

Results of the bulkhead test panel finite element analyses for each the four materials considered were examined in terms of plate displacement profiles, maximum plate displacements, von Mises stress distributions and the total dissipated energy in the plate material interior to the stiffener boundaries.

Under increasing hydrostatic pressure the central square portion of each plate, bounded by the T-stiffeners, exhibited extensive deformation out of the undeformed panel plane (Figure 5). The T-stiffeners and the plate region between the T-stiffener and the test fixture sustained considerably less deformation than the central portion of the panel. The maximum deflection developed, as anticipated, at the center of the bulkhead test panel.

The applied hydrostatic pressure versus center plate deflection is plotted in Figure 6. The center plate deflection, for the four materials considered here, responded similarly below 500 psi for all panels. The two 80 ksi yield strength panel responses departed from the two 100 ksi yield strength panel responses above 500 psi as plasticity, governed by initial material yield, develops.

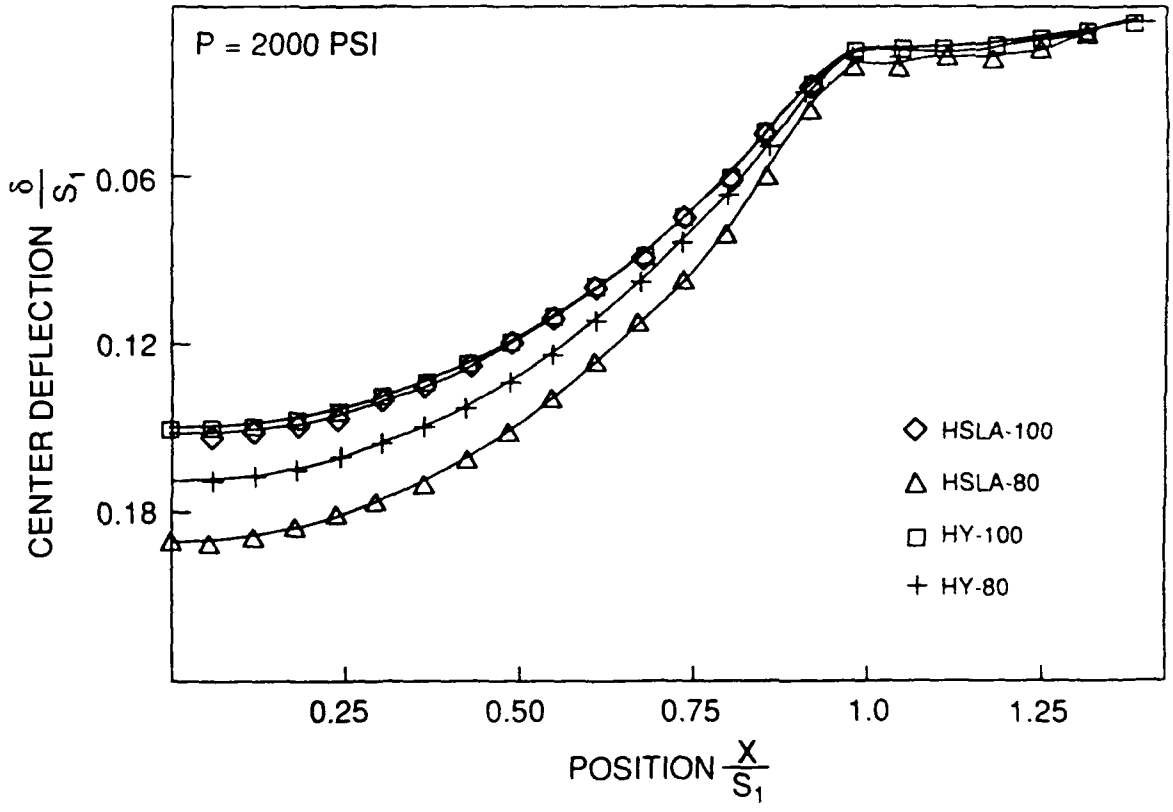

Fig. 5 — Plate displacement profile along x (or y) axis for HY-80, HY-100, HSLA-80 and HSLA-100 materials at applied hydrostatic pressure load of 2000 psi

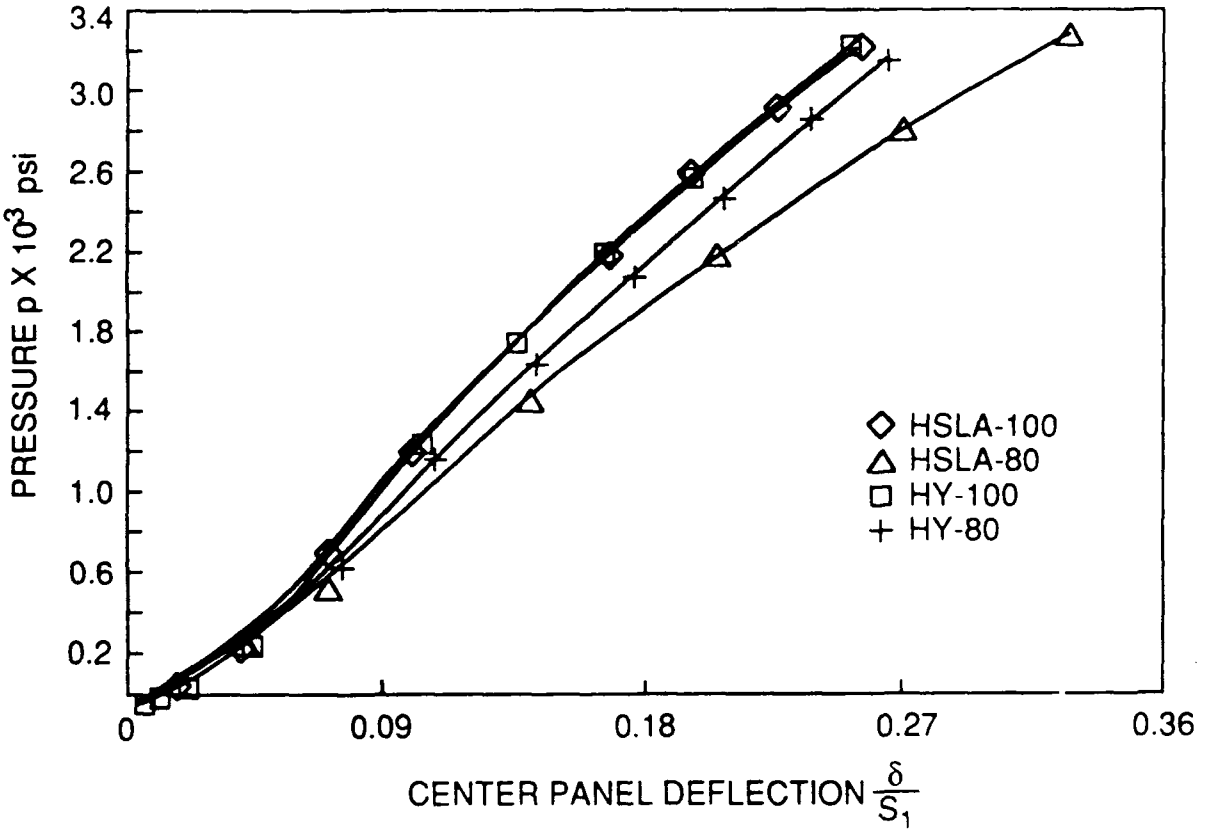

Fig. 6 — Applied hydrostatic pressure versus vertical deflection at center of plate for HY-80, HY-100, HSLA-80 and HSLA-100 material

The deflection responses predicted for the HY-100 and HSLA-100 panels remain essentially identical for the entire range of applied hydrostatic pressure, from 0 to over 3000 psi, considered in the analysis. Predictions for both materials exhibited the overall stiffest response and smallest center deflections for a specified pressure.

The deflection responses of the HY-80 and HSLA-80 panels were predicted to diverge slowly but consistently for pressures exceeding 1000 psi. The HSLA-80 panel response was predicted to be the most compliant and exhibited the largest center deflections. The HY-80 panel exhibited a somewhat stiffer response than the HSLA-80 panel, but more compliant than the HY-100 and HSLA-100 panels.

The general shape of all four pressure versus deflection responses were observed to be similar. All were concave, indicative of a stiffening in global response, below a pressure of approximately 900 psi. All were convex, indicative of a softening in global response, above a pressure of approximately 1200 psi. The inflection points in the pressure versus deflection response curves, corresponding to the transition between the concave and convex regions, developed at pressures of approximately 900 psi for HY-80, 1000 psi for HY-100, 1100 psi for HSLA-80 and 1200 psi for HSLA-100.

In order to examine the stress, strain and energy fields producing this behavior in more detail, the deflected shapes and von Mises stress fields of the shell model were plotted below and above the transition pressures associated with the concave and convex portions of the applied hydrostatic pressure versus center displacement responses. Results below the transition range are shown in Figure 7 for the HY-80, HY-100, HSLA-80 and HSLA-100 analyses at applied hydrostatic pressures of 648, 722, 558 and 678 psi, respectively. (These pressures correspond to those solution increments near, but below, the transition.) Yield stress was the dominant factor governing the differences in plate and stiffener stress distributions. The global deflections, and therefore the local strains, were comparable at this level of deformation for the material pairs of similar yield stress.

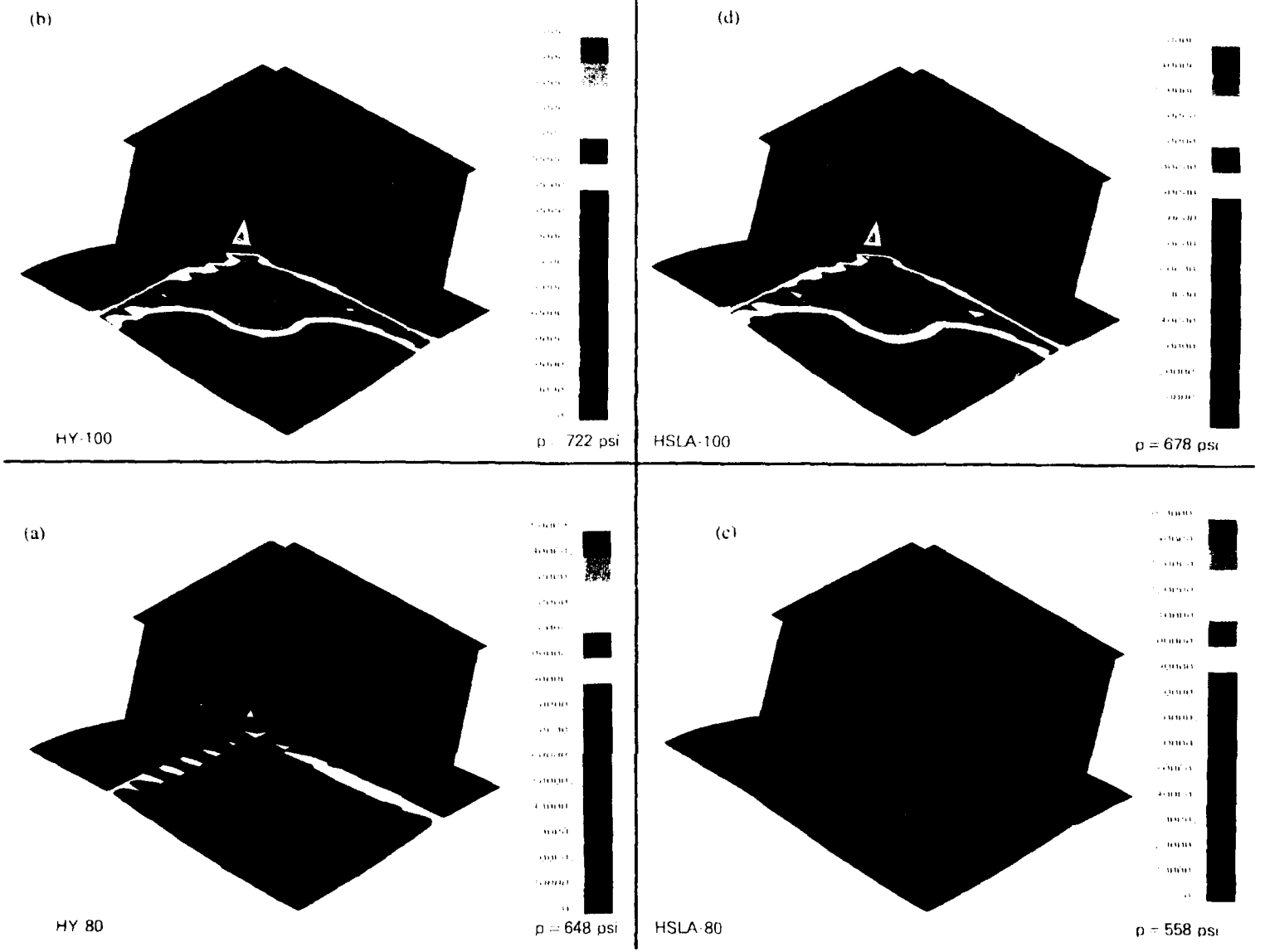

Fig. 7 – Deflected shape and von Mises stress field of bulkhead test panel below the applied hydrostatic pressure load versus center displacement response transition for (a) HY-80, (b) HY-100, (c) HSLA-80 HSLA-80 and (d) HSLA-100 material

Results above the transition range are shown in Figure 8 for the HY-80, HY-100, HSLA-80 and HSLA-100 analyses at applied hydrostatic pressures of 2060, 2180, and 2180 and 2060 psi, respectively. In this case, the relative differences between panel responses were produced not only by relative differences in yield stress but also by the relative differences in post yield response of the materials. In particular, through moderate uniaxial logarithmic strains of approximately 0.30, the tangent modulus of the HY materials was significantly greater than the initial hardening of the HSLA materials. Beyond this level of strain, the tangent modulus of the HY materials decreased very rapidly when compared to the HSLA class of materials. The HSLA materials, on the other hand, offered a more uniform resistance to plastic deformation over a broader range of effective plastic strains. This, in turn, produced a more uniform deformation. This was particularly evident for HSLA-80.

As a result of these differences in tangent modulus at intermediate and larger strains, the HY materials were initially somewhat more resistant to plastic deformation. After the tangent modulus decreases, however, plastic deformation proceeds with considerably less additional stress incrementation. In the vicinity of the circular zone of low von Mises stresses inscribing the stiffener boundary, the panel geometry and hydrostatic loading produced more severe von Mises stress gradients in the plate. These gradients were considerably more severe in the HY materials than the HSLA materials. The difference is somewhat greater between HY-80 and HSLA-80 panels since the difference in tangent modulus is also greater for intermediate strains. This low stress zone is spatially continuous through moderate deformations. For the 100 ksi materials at 2000 psi applied hydrostatic pressure, however, the zone continuity is broken in the HY-100 plate but still intact in the HSLA-100 plate. Breakdown of this zone leads to localization of deformation at the web and plate intersection and produces less uniform deformation over the plate as a whole.

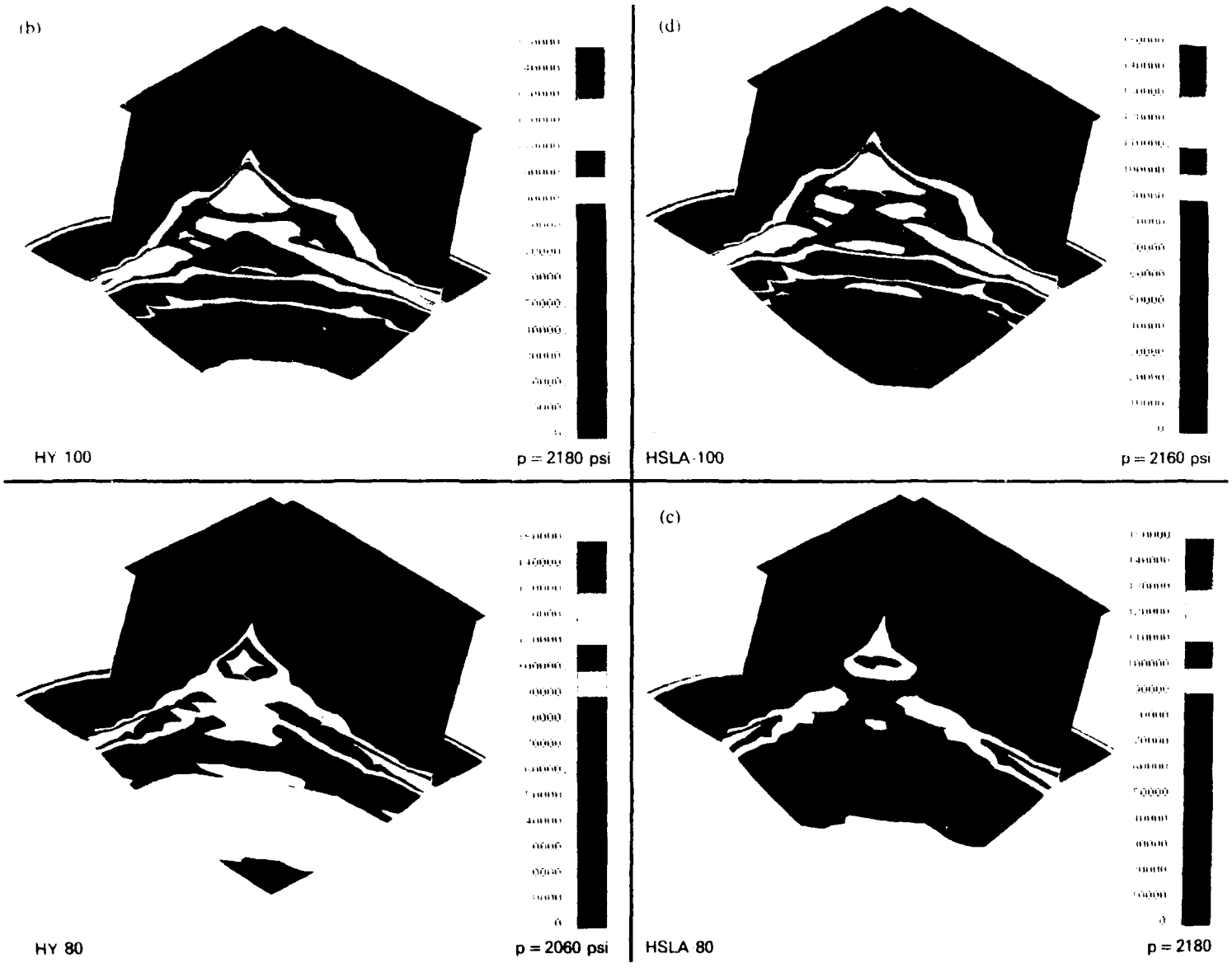

Fig. 8 — Defected shape and von Mises stress field of bulkhead test panel above the applied hydrostatic pressure load versus center displacement response transition for (a) Hy-80, (b) HY-100, (c) HSLA-80 and (d) HSLA-100 material

The energy W absorbed by the square region of plate material inside the stiffener boundary was determined from the finite element analysis. The HSLA-80 plate absorbed more energy than the other three plates. At an applied pressure of approximately 2100 psi, the energy absorbed by the HY-80, HY-100 and HSLA-100 plate was 77, 71 and 76 percent of the HSLA-80 plate, respectively. These proportions suggested very similar energy absorbing characteristics for the HY-80, HY-100 and HSLA-100 plates and an approximately thirty per cent greater ability for the HSLA-80 plate to absorb energy.

Web-Plate Detail Continuum Model

The shell model results provided information on the large scale response of the test panel. Of particular interest was the response of the cross section of the plate and web perpendicular to the stiffener at the midside of the stiffener. At this location, the shell model von Mises stress field results indicated a secondary concentration of plastic deformation. The geometry of the plate and web intersection were anticipated to produce a more severe state of local deformation than indicated by the shell model. To address this issue, a more refined local finite element model of the plate and web intersection at the midside location was developed (Figure 9).

The intersection, as a welded connection, was also a source of material inhomogeneity and geometric flaws. For the purposes of this investigation, the intersection was considered to be entirely of base metal. The weld geometry for the intersection was known, however, and the integrity of the intersection to the presence of flaws was considered. Of particular interest were the resistance to crack growth of flaws on the upper surface of the plate,inside the stiffener periphery at the toe of the weld. Web and plate intersection models were developed for the flaw free geometry and for one flaw size, a, extending into the plate thickness, t_1, at the toe of the weld geometry to an a/t_1 ratio of 0.14. Each model was analyzed for each of the four steel alloys under consideration.

The vertical deflection of the plate at the web and plate intersection, as seen in Figure 5, was relatively small in comparison to the stiffener dimension s_1. The resulting out-of-plane deformation at the stiffener midside produced an associated out-of-plane strain component that was on the order of the material yield strain. This

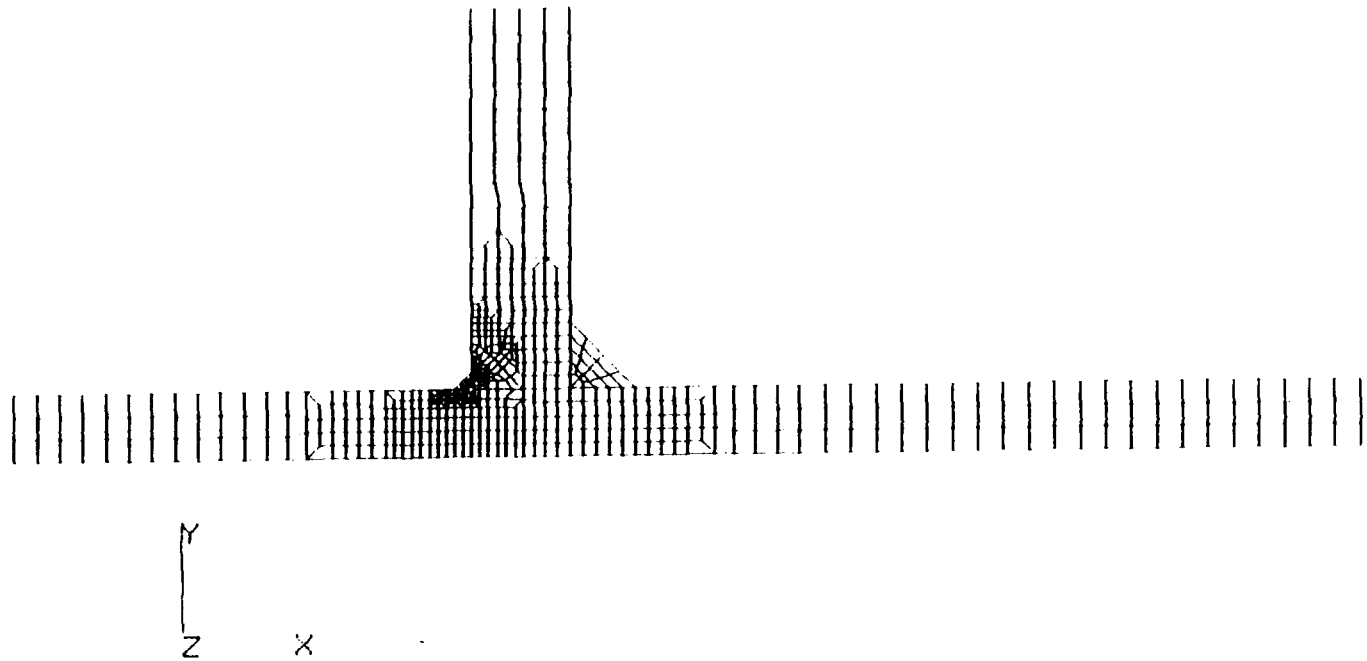

Fig. 9 — Plane strain finite element model of T-frame stiffener and plate intersection geometry

strain magnitude, when compared to in-plane strain components associated with the extensive yielding present in the plate material, was sufficiently small to justify a plane strain approximation of the deformation in the immediate vicinity of the intersection. This observation also held for the stiffener and for plate material between the intersection and plate periphery at the midside location. The out-of-plane strains increased to a few percent at the detail model location nearest to the center of the of the plate. These strain magnitudes remained sufficiently small in comparison to in-plane strain components and remote from the intersection itself. As discussed earlier, the extent of the detail model was selected to ensure that length scales were sufficiently greater than the thickness scales. Therefore, detail model loading was sufficiently remote from the intersection itself. Detail model boundaries were coincided with shell model element boundaries to facilitate implementation of applied displacements to the detail model.

On the basis of these strain magnitudes, two dimensional web-plate intersection models were developed utilizing plane strain elements of type CPE8. The flaw free model contained 1837 nodes composed into 548 elements. Additional pairs of nodes were introduced to generate the additional surfaces required for the flaw geometry model. The total number of degrees of freedom in the model was 3674.

Displacement boundary conditions for each material used in the three continuum models were derived from the shell model nodal translational and rotational results. The material boundaries of the continuum model, i.e. the left side of the plate and the upper side of the web, were displaced according to the shell model results. The right side of the plate in the model corresponded to the plate and fixture intersection and was constrained to zero displacement along the plate thickness boundary. Physically, hydrostatic pressure was present on the upper surfaces of the plate and web of the intersection model. The stresses produced by the hydrostatic pressure were significantly smaller than those produced by the displacement boundary conditions associated with the membrane and bending deformations obtained from the shell model. Therefore, only the displacement loading was used in intersection models.

Web-Plate Detail Model Results

The web and plate intersection detail model were also analyzed for each of the four materials considered. The role of plastic deformation in these regions on the observed center plate displacements was of particular interest in view of the pressure versus displacement transitions obtained from the panel models.

The von Mises stress field of the web and plate intersection are shown on the deflected shape of the intersection prior to the global stiffness transition in Figure 10 for the HY-80, HY-100, HSLA-80 and HSLA-100 analyses at displacement loading corresponding to applied hydrostatic pressures of 775, 800, 500 and 652 psi, respectively. (As noted earlier, the selection of these pressures corresponded to those solution increments near, but below, the pressure versus center displacement transition.) At these lower pressures, the deformations were qualitatively similar and show the onset of deformation concentration at the web and plate intersection.

Plots of the intersection subsequent to the transition to a more compliant response are shown in Figure 11 for the HY-80, HY-100, HSLA-80 and HSLA-100 pressures of 2075, 2006, 2089 and 2015 psi. At the higher pressures, differences were evident between the relative curvatures of the plate deformation, immediately adjacent to the stiffener boundary, and the relative curvature of the plate, interior to the stiffener, located a few plate thicknesses from the intersection. This curvature, in conjunction with the effects of the weld geometry, produced locally intense stress, strain and energy density fields at the weld geometry toe. If the adjacent plate material deformed in such a way as to distribute the deformation, a smooth transition was provided to the deformation in the central region of the plate. The resulting load redistribution would suppress development of intense plastic deformation at the intersection. This was seen for the 80 ksi yield materials in the relatively low stress level which was produced in the HSLA-80 plate compared to the HY-80 plate. For the 100 ksi materials, the effect was less pronounced. It was seen, however, as a more local effect attenuating the degree of through thickness yielding at the intersection in the HSLA-100 plate versus the HY-100 plate. As a result of these effects, the tendency for fracture initiation to occur would also be suppressed. Failure of the material to produce a smooth transition in turn produced a more rigid rotation of the plate material, further intensifying the deformation at the weld toe and leading to a response essentially equivalent to a plastic hinge. The through thickness contraction of the HY-100 plate at the intersection is evidence of this having occurred.

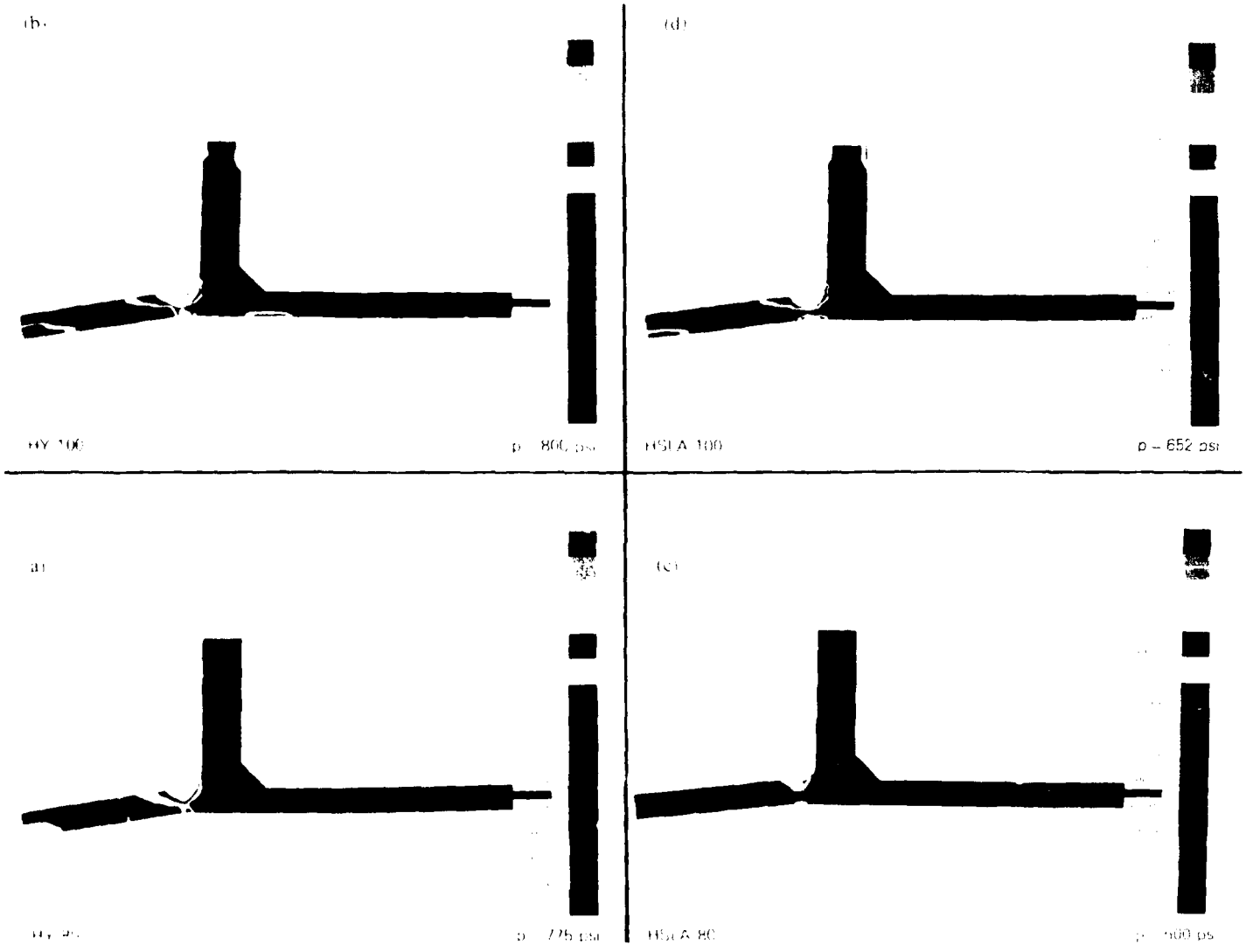

Fig. 10 — Deflected shape and von Mises stress field of web and plate intersection geometry below the applied hydrostatic pressure versus plate center displacement transition for (a) HY-80, (b) HY-100, (c) HSLA-80 and (d) HSLA 100 material

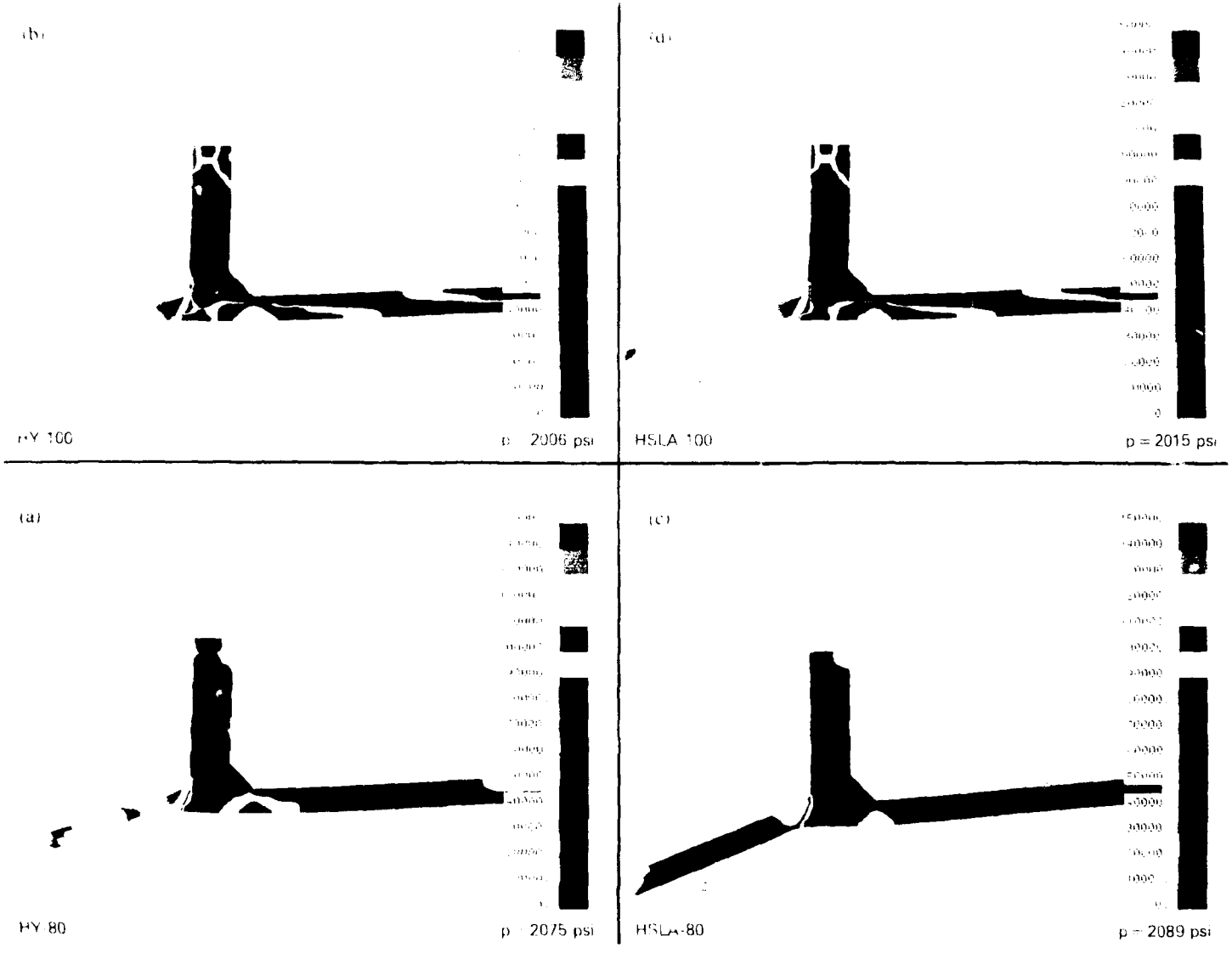

Fig. 11 - Deflected shape and von Mises stress field of web and plate intersection geometry above the applied hydrostatic pressure versus plate center displacement transition for (a) HY-80, (b) HY-100, (c) HSLA-80 and (d) HSLA-100 material

The tendency of the web and plate intersection material to absorb energy was examined by plotting the absorbed energy density versus applied hydrostatic pressure at the finite element integration point nearest to the weld geometry toe (Figure 12). The data from the additional series of analyses on the flawed geometry, at the finite element integration point nearest the crack tip, was plotted in (Figure 13).

The critical strain energy density values were reached in the HY-80 and HY-100 analyses. Crack growth would be predicted to commence at pressures of 2180 and 2220 psi, respectively, for the flaw free plate and 1980 and 1900 psi, respectively, for the flawed plate. The critical strain energy density values exceeded the strain energy density values attained in the HSLA-80 and HSLA-100 analyses for both the flaw free and flawed geometries. The critical pressures could be anticipated at approximately 2500 and 2400 psi, respectively, based on the trends through the pressure range analyzed. The introduction of the crack decreased the critical pressures by just under ten percent. The energy density response could also be used to specify the minimum material fracture toughness requirement which a material must satisfy for a specified pressure.

The relative resistance of the intersection to fracture initiation is shown in Figures 14 and 15 by normalizing the absorbed energy with respect to the local fracture toughness of the panel material. Quantitative differences in material performance in both flaw free and flawed geometry is apparent despite the relative similarities in energy density histories at the crack tip of each material.

Weld material, welding process and fabrication practice are all important aspects not considered in this investigation. The concepts utilized here apply to both the fracture initiation prediction and minimum required toughness specification if the constitutive responses of the specific weld materials and heat affected zones are known and included in the model.

Conclusions

Computational simulations of a T-stiffened bulkhead test panel to hydrostatic pressure loading were conducted for HY-80, HY-100, HSLA-80 and HSLA-100 steel alloys. Large scale panel performance for each material was obtained using

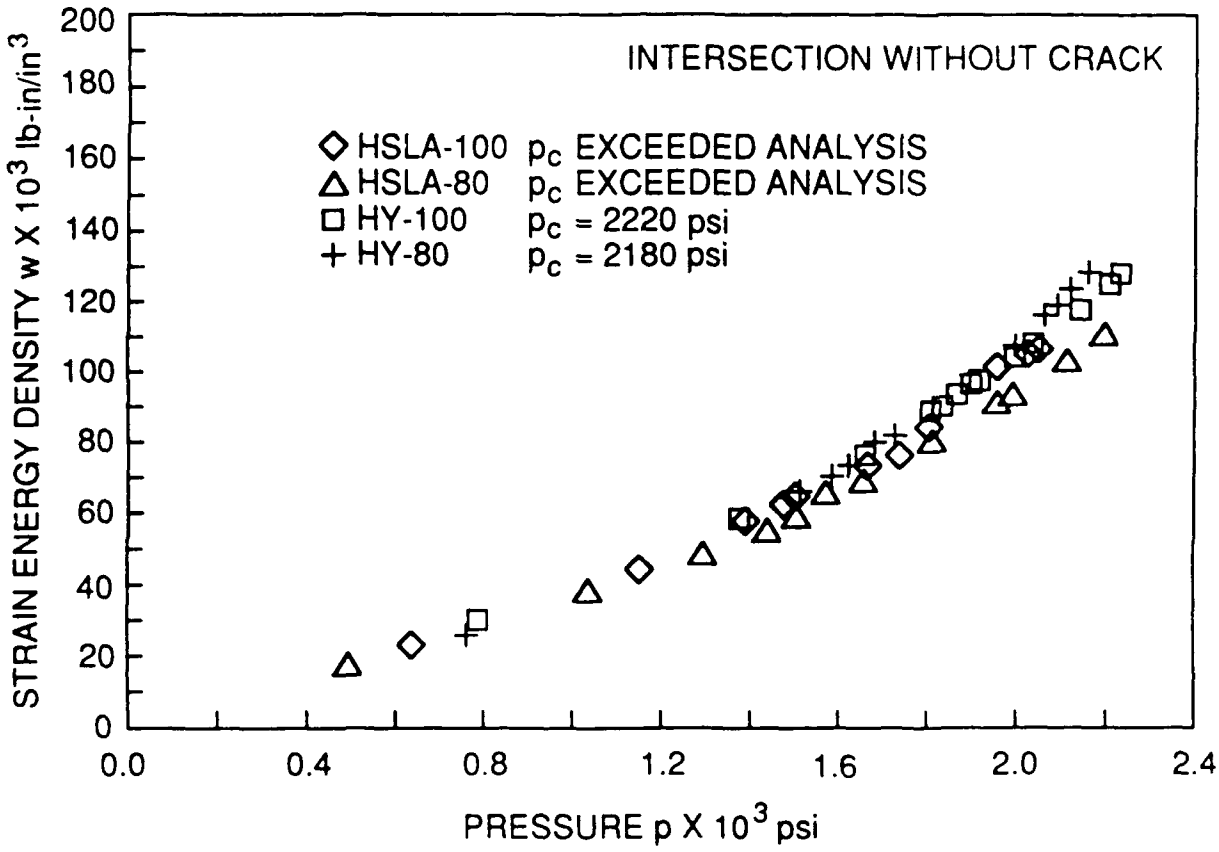

Fig. 12 — Absorbed strain energy density versus applied hydrostatic pressure for flaw free web and plate intersection for HY-80, HY-100, HSLA-80 and HSLA-100 materials

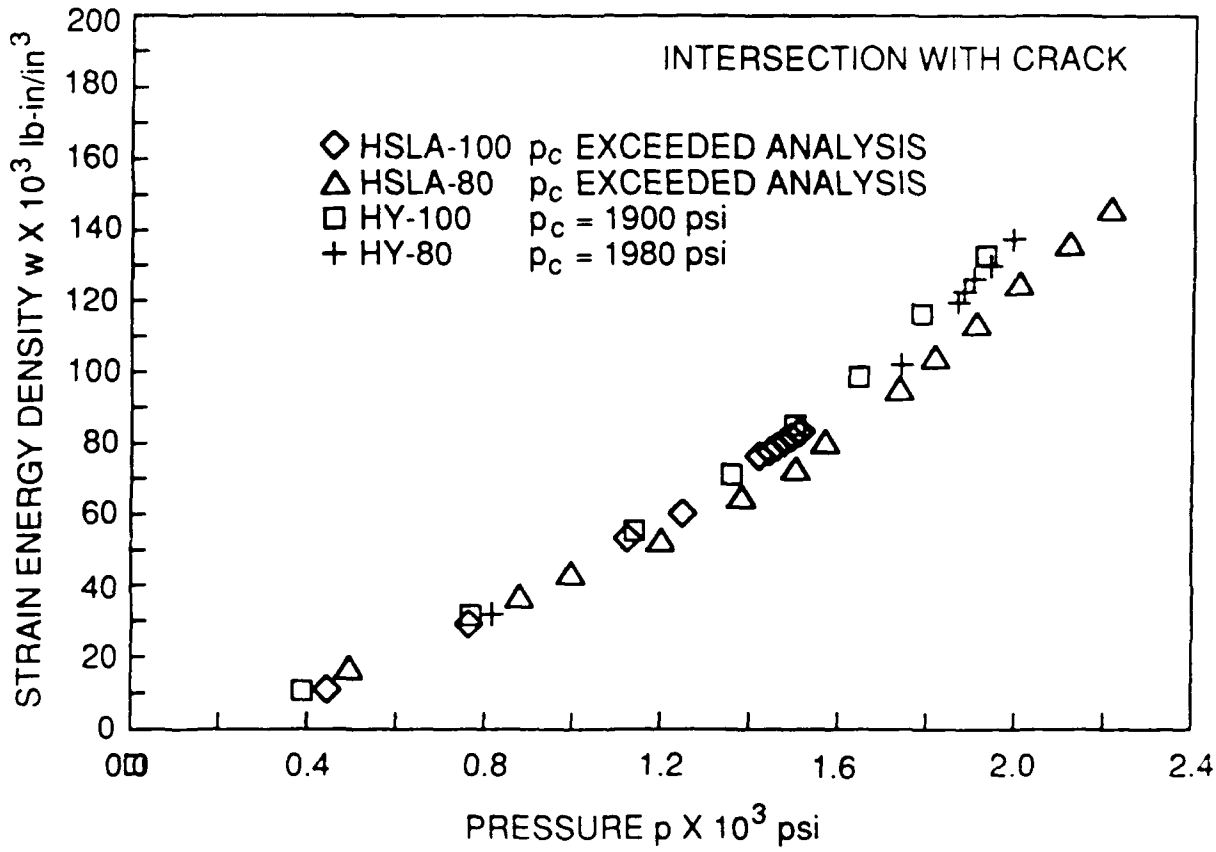

Fig. 13 — Absorbed strain energy density versus applied hydrostatic pressure near crack tip at web and plate intersection for HY-80, HY-100, HSLA-80 and HSLA-100 materials

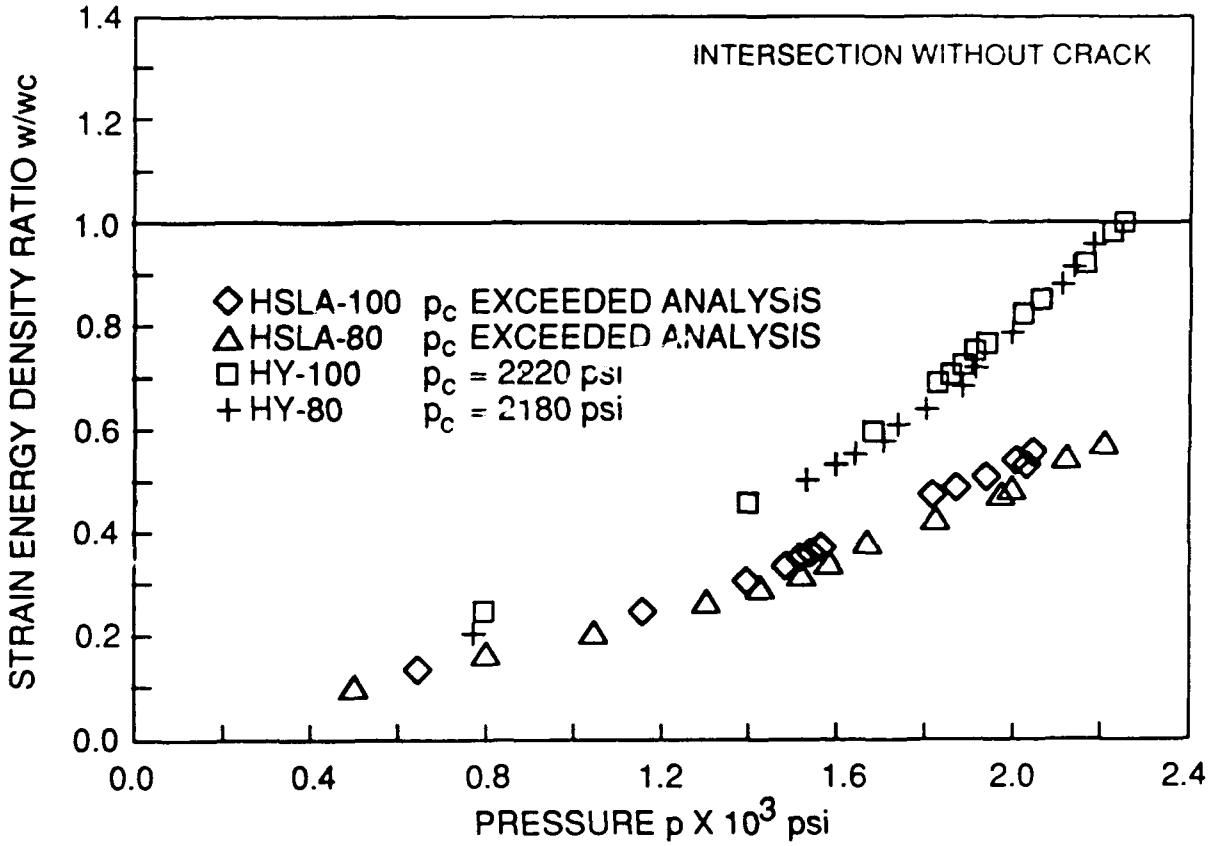

Fig. 14 — Critical strain energy density ratio versus applied hydrostatic pressure for flaw free web and plate intersection for HY-80, HY-100, HSLA-80 and HSLA-100 materials

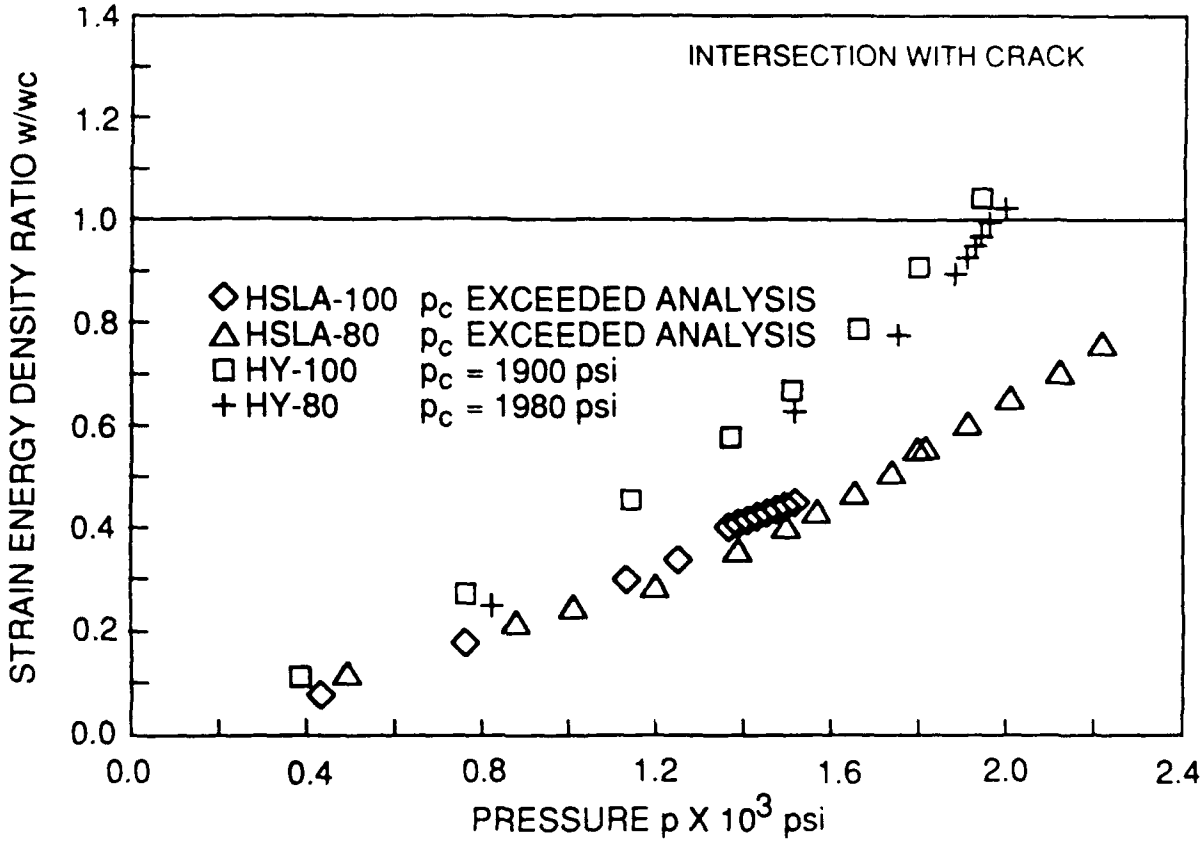

Fig. 15 — Critical strain energy density versus applied hydrostatic pressure near crack tip at web and plate intersection for HY-80, HY-100, HSLA-80 and HSLA-100 materials

nonlinear shell finite elements. Detailed analysis of the web and plate intersection performance was obtained using nonlinear continuum finite elements.

The nonlinear constitutive response and local fracture toughness of each material were observed to influence the nature and extent of global panel deformation and energy dissipation. Relative differences in the stiffening and softening of the test panel were predicted. Material yield stress influences the onset of stiffening, while large strain nonlinearity in the material influences the onset of softening. These differences suggest that the four alloys considered offer distinct choices in panel performance. The use of plastic dissipation in the square panel region interior to the stiffeners provided an additional quantitative measure of plate performance.

From these perspectives, the higher yield strength materials, i.e. HY-100 and HSLA-100, were superior materials in terms of the sustained panel stiffness associated with their responses. The lower yield strength materials, i.e. HY-80 and HSLA-80, demonstrated an enhanced ability to dissipate energy in the panel geometry. Between these two materials, HSLA-80 sustained relatively uniform deformation in comparison to HY-80. By avoiding deformation localization in this manner, the HSLA-80 was able to dissipate considerably more energy.

The global performance was determined to be strongly dependent on the degree of deformation localization in the plate and at the web and plate intersection. Detailed analysis of the intersection provided insight into the role of the weld geometry on deformation localization. Flaw tolerance at the intersection was also assessed for a crack depth fourteen percent of the plate thickness. The effect of the flaw was found to be relatively insignificant, reducing the critical pressure for crack growth initiation by ten percent, for the homogeneous material system. Conversely, the energy density response also specifies minimum material fracture toughness requirements for a specified pressure. The actual effects of weld material and weld process on flaw tolerance must be addressed by explicit consideration of the weld constitutive and local fracture toughness.

Computational capabilities to resolve both large scale and small scale component response may suggest additional methods to assess performance. The relative merit of each material may benefit from both a global and a local perspective. The applied load, average deflection and net energy dissipation provide global performance

measures. The most severe stress states, strain states and dissipated energy densities provide parallel measures of local performance.

Many factors enter into the decision of material selection. Parallel considerations pertaining to shock response, corrosion and fabrication must also be accounted for and the relative merits of each weighed against one another. The ability to computationally investigate the alternatives offers unique opportunities, however, governed by the generality of the methodology and the accuracy of the data required for analysis.

Acknowledgements

The authors wish to acknowledge the support of the David Taylor Research Center and the Office of Naval Technology.

References

[1] ABAQUS Theory Manual, Hibbitt, Karlsson and Sorensen, Inc., Providence, RI, 1984.

[2] Wong, A. K., G. C. Kirby III and P. Matic, "A Hybrid Experimental-Computational Scheme for Determining Stress-Strain Data Under Large Strains," NRL Memo Report (In preparation).

[3] Matic, P., G. C. Kirby III and M. I. Jolles, "The Relation of Tensile Specimen Size and Geometry Effects to Unique Constitutive Parameters for Ductile Materials," Proc. Roy. Soc. Lond., Vol. A 417 (1988), pp 309-333.

[4] Matic, P., P.R. Father, G. C. Kirby III and M. I. Jolles, "Determination of Ductile Alloy Constitutive Response by Iterative Finite Element and Laboratory Video Image Correlation," NRL Memo Report 6233 (1988).

[5] Wong, A. K., G. C. Kirby III and P. Matic, "Elastic-Plastic Stress-Strain Characterization to Fracture of HSLA-100 Steel," NRL Memo Report (In preparation).

[6] ABAQUS User's Manual, Hibbitt, Karlsson and Sorensen, Inc., Providence, RI, 1984.